



Sensitivity of ^{44}Ti and ^{56}Ni Production in Core-collapse Supernova Shock-driven Nucleosynthesis to Nuclear Reaction Rate Variations

Shiv K. Subedi¹, Zach Meisel¹, and Grant Merz¹

Institute of Nuclear & Particle Physics, Department of Physics & Astronomy, Ohio University, Athens, OH 45701, USA; ss383615@ohio.edu, meisel@ohio.edu

Received 2020 February 25; revised 2020 May 16; accepted 2020 May 26; published 2020 July 16

Abstract

Recent observational advances have enabled high resolution mapping of ^{44}Ti in core-collapse supernova (CCSN) remnants. Comparisons between observations and models provide stringent constraints on the CCSN mechanism. However, past work has identified several uncertain nuclear reaction rates that influence ^{44}Ti and ^{56}Ni production in postprocessing model calculations. We evolved one-dimensional models of $15 M_{\odot}$, $18 M_{\odot}$, $22 M_{\odot}$, and $25 M_{\odot}$ stars from zero age main sequence through CCSN using Modules for Experiments in Stellar Astrophysics and investigated the previously identified reaction rate sensitivities of ^{44}Ti and ^{56}Ni production. We tested the robustness of our results by making various assumptions about the CCSN explosion energy and mass cut. We found a number of reactions that have a significant impact on the nucleosynthesis of ^{44}Ti and ^{56}Ni , particularly for lower progenitor masses. Notably, the reaction rates $^{13}\text{N}(\alpha, p)^{16}\text{O}$, $^{17}\text{F}(\alpha, p)^{20}\text{Ne}$, $^{52}\text{Fe}(\alpha, p)^{55}\text{Co}$, $^{56}\text{Ni}(\alpha, p)^{59}\text{Cu}$, $^{57}\text{Ni}(n, p)^{57}\text{Co}$, $^{56}\text{Co}(p, n)^{56}\text{Ni}$, $^{39}\text{K}(p, \gamma)^{40}\text{Ca}$, $^{47}\text{V}(p, \gamma)^{48}\text{Cr}$, $^{52}\text{Mn}(p, \gamma)^{53}\text{Fe}$, $^{57}\text{Co}(p, \gamma)^{58}\text{Ni}$, and $^{39}\text{K}(p, \alpha)^{36}\text{Ar}$ are influential for a large number of model conditions. Furthermore, we found the list of influential reactions identified by previous postprocessing studies of CCSN shock-driven nucleosynthesis is likely incomplete, motivating future larger-scale sensitivity studies.

Unified Astronomy Thesaurus concepts: [Astrophysical explosive burning \(100\)](#); [Explosive nucleosynthesis \(503\)](#); [Core-collapse supernovae \(304\)](#)

1. Introduction

Stars with initial mass $\gtrsim 8 M_{\odot}$ undergo a core-collapse supernova (CCSN) explosion after core fuel exhaustion (Woosley & Janka 2005). The CCSN enriches the interstellar medium by releasing the isotopes synthesized throughout its life cycle and during CCSN nucleosynthesis. Among the ejected isotopes, ^{44}Ti and ^{56}Ni are produced near the boundary of the protoneutron star remnant and the ejecta, and are thus studied to gain insight into details of the CCSN mechanism (Young et al. 2006; Young & Fryer 2007; Fryer et al. 2012, 2018).

Observations of ^{44}Ti in CCSN remnants are possible due to characteristic γ -rays at 67.9, 78.3, and 1157.0 keV emitted in the decay sequence ^{44}Ti ($t_{1/2} = 59.1$ yr) \rightarrow ^{44}Sc ($t_{1/2} = 3.97$ hr) \rightarrow ^{44}Ca (stable) (Chen et al. 2011). ^{56}Ni , on the other hand, follows the much briefer decay sequence ^{56}Ni ($t_{1/2} = 6.08$ day) \rightarrow ^{56}Co ($t_{1/2} = 77.2$ day) \rightarrow ^{56}Fe (Junde et al. 2011). As such, CCSN ^{56}Ni production is generally inferred from observations of the remnant iron, e.g., for the Cassiopeia A (CasA) supernova of 1671 AD (Eriksen et al. 2009).

Comparing such observational constraints to yields from CCSN model calculations offers the opportunity to constrain properties of the CCSN explosion, such as the explosion energy and duration, as well as the remnant mass (Aufderheide et al. 1991; Young et al. 2006; Young & Fryer 2007; Müller et al. 2017; Fryer et al. 2018; Sawada & Maeda 2019). However, model calculation results for ^{44}Ti and ^{56}Ni yields have been shown to have significant sensitivities to variations in nuclear reaction rates (The et al. 1998; Hoffman et al. 1999; Magkotsios et al. 2010). This is particularly problematic as many of the relevant reaction rates have poor experimental

constraints. Nuclear physics measurements can be prioritized with the aid of sensitivity studies, whereby nuclear reaction rates are varied within an uncertainty factor and the impact on the model calculation results is assessed.

Large-scale investigations of nuclear reaction rate uncertainties impacting shock-driven nucleosynthesis in CCSN were previously performed by The et al. (1998) and Magkotsios et al. (2010). These pioneering works used analytic temperature–density trajectories in nucleosynthesis postprocessing calculations, varying nuclear reaction rates by factors of $/100$ and $\times 100$. They identified several nuclear reaction rates that can impact ^{44}Ti and ^{56}Ni nucleosynthesis for temperature and density trajectories approximating material heated by the expanding shock following a supernova core bounce. We build on prior work in the following ways. (1) We perform stellar evolution and CCSN calculations with one-dimensional models in an effort to focus on astrophysical conditions that are most relevant to comparisons with astronomical observations. (2) We vary nuclear reaction rates by realistic rate variation factors based on existing nuclear physics constraints in order to avoid focusing on cases which are already sufficiently constrained. (3) We cross-check whether the prioritized reaction rate lists resulting from prior studies are comprehensive. We note that similar work has been done by Hoffman et al. (2010) and Tur et al. (2010), but for a much smaller set of reaction rate variations.

Our paper is organized as follows. In Section 2 we discuss the model details for massive star evolution and subsequent CCSN. In Section 3 we detail temperature and density evolution during CCSN for comparison with prior postprocessing work. In Section 4 we present the explosion details, nucleosynthetic yields of ^{44}Ti and ^{56}Ni from our baseline CCSN calculations, and compare to yields determined by observations and previous modeling efforts. In Section 5 we

¹ Affiliated with the Joint Institute for Nuclear Astrophysics–Center for the Evolution of the Elements.

present our list of varied reaction rates and adopted reaction rate variation factors. In Section 6 we present nuclear physics sensitivities, explaining the rate impacts in terms of the nuclear reaction network. In Section 7 we compare our results with the postprocessing calculations of The et al. (1998) and Magkotsios et al. (2010). We conclude in Section 8, with brief suggestions for future work involving astrophysics model calculations and nuclear physics experiments.

2. MESA Calculations

We performed one-dimensional, multizone model calculations using Modules for Experiments in Stellar Astrophysics² (MESA), which is an open-source code for modeling stellar evolution and stellar explosions (Paxton et al. 2011, 2015, 2018, 2019). In order to perform CCSN, we ran our simulations in two different stages using MESA version 7624, consisting of evolution to core collapse followed by the supernova explosion.

In stage one, we evolved nonrotating, solar metallicity ($Z = 0.02$) $M_{\text{prog}} = 15 M_{\odot}$, $18 M_{\odot}$, $22 M_{\odot}$, and $25 M_{\odot}$ progenitors from zero age main sequence (ZAMS) to the onset of core-collapse, as this is within the suspected ZAMS mass range for progenitors of CCSN remnants with observed ^{44}Ti (Pérez-Rendón et al. 2002; Young et al. 2006; Wongwathanarat et al. 2017). Our stage one calculations are based on Farmer et al. (2016), using the 204 isotope network `mesa_204.net`,³ the JINA ReacLib reaction rate library version V2.0 2013-04-02 (Cyburt et al. 2010), and the Dutch wind scheme that is based on Nieuwenhuijzen & de Jager (1990), Nugis & Lamers (2000), Vink et al. (2001), and Glebbeek et al. (2009) with an efficiency scale factor $\eta = 0.8$ (Maeder & Meynet 2001). The spatial resolution resulted in the number of zones varying between ~ 450 and 1200 zones, with the number of zones tending to increase in later stages of stellar evolution. The onset of core-collapse was defined as the time when any mass zone at the interior of the star exceeded an infall velocity of 1000 km s^{-1} (Farmer et al. 2016).

Stage two took the final stellar model of stage one and carried this into the CCSN phase, following the procedure described by Paxton et al. (2015), which is divided into four distinct steps:

1. Run MESA using `inlist_adjust`, where we adjust several control parameters for initiating CCSN simulations. The astrophysical parameters were chosen following Farmer et al. (2016). Notable among them are absence of any prescription to mimic rotation and the choice of the Dutch wind scheme with $\eta = 0.8$.
2. Run MESA using `inlist_remove_core`, where we define and remove the stellar core. The outer mass coordinate of the core, i.e., the deepest zone of the model, is defined by the inner mass boundary I_b , located at the mass coordinate just outside the Fe core (as specified in Table 1).
3. Run MESA using `inlist_edep`, which employs the “thermal bomb” mechanism (e.g., Young & Fryer 2007; Paxton et al. 2015) to inject energy $E_{\text{inj}} \sim 10^{51} \text{ erg}$ (Fryer et al. 2012) into a thin mass shell $\Delta M_{\text{shell}} = 0.05 M_{\odot}$ above I_b (the innermost ~ 20 zones) over a time

period $t_{\text{inj}} = 20 \text{ ms}$. As specified in Table 1, we inject $E_{\text{inj}} = 0.5 \text{ foe}^4$ in $15 M_{\odot}$ and $18 M_{\odot}$ models; 1.32 foe in $15 M_{\odot}$, $18 M_{\odot}$, and $22 M_{\odot}$; and 3.5 foe in $22 M_{\odot}$ and $25 M_{\odot}$ ZAMS stars. These explosion energies were roughly based on the findings of Vartanyan et al. (2019), Fryer et al. (2012), Paxton et al. (2015), and Nomoto (2014), where the specific energies were somewhat arbitrarily chosen in order to span a plausible range.

We limited ourselves to a single t_{inj} to keep the overall number of calculations manageable. Our choice of t_{inj} was motivated in part by the finding of Fryer et al. (2012) that most supernovae have explosion energies $E_{\text{exp}} > 10^{51} \text{ erg}$, which can be reached if the explosion occurs less than 250 ms after core bounce. Additionally, the analysis of Sawada & Maeda (2019) suggests short explosion timescales are more consistent with observations. The specific choice of $t_{\text{inj}} = 20 \text{ ms}$ corresponds to the fast-explosion timescale for thermal bomb models explored in Young & Fryer (2007). To explore the impact of this choice, we performed CCSN calculations for the $18 M_{\odot}$ model using $E_{\text{inj}} = 1.32 \text{ foe}$ and $t_{\text{inj}} = 3, 20$, and 200 ms , comparing the yield of ^{44}Ti (see Section 4). The 20 ms calculations were in closer agreement with the ^{44}Ti yields of 3D models and observations, further motivating our choice. Similarly, we explored using $\Delta M_{\text{shell}} = 0.02 M_{\odot}$, finding little impact on the ^{44}Ti and ^{56}Ni yields.

4. Run MESA using `inlist_explosion`, which follows the thermodynamic and nucleosynthetic evolution of the stellar envelope due to the shock wave propagating outward from the thermal bomb energy deposition region. Nuclear reaction rates were varied in this step of the calculations.

3. Evolution of Temperature and Density during CCSN

As the shock wave powered by the thermal bomb propagates toward the stellar surface, it changes the thermodynamic conditions in the regions of the star that it sweeps through. We quantify the impact on thermodynamic conditions by comparing to analytic temperature–density trajectories, namely exponential and power law, often used in postprocessing studies (e.g., The et al. 1998; Magkotsios et al. 2010). Both trajectories are characterized by a peak temperature T_0 and peak density ρ_0 , followed by expansion and cooling with constant $T^3 \rho^{-1}$ (Magkotsios et al. 2010).

The exponential trajectory is based on Fowler & Hoyle (1964), where material heated to T_0 and compressed to ρ_0 undergoes adiabatic expansion, and the expansion timescale τ is equal to the freefall timescale:

$$\tau = (24\pi G \rho_0)^{-1/2} \approx 446(\rho_0)^{-1/2} \text{ s}, \quad (1)$$

where G is Newton’s gravitation constant. The associated temporal evolution of temperature and density are described by Magkotsios et al. (2010), Harris et al. (2017), and

² <http://mesa.sourceforge.net>

³ Magkotsios et al. (2010) found this network size is sufficient for the temperature and density phase space and initial Y_e relevant for our work.

⁴ 1 foe = 10^{51} erg .

Table 1
Key Model Properties and the Resultant $M(^{44}\text{Ti})$ and $M(^{56}\text{Ni})$ with $\Delta M_{\text{shell}} = 0.05 M_{\odot}$ for the Baseline Calculations Performed in This Work

M_{prog} (M_{\odot})	E_{inj} (foe)	E_{exp} (foe)	Fe_{core} (M_{\odot})	I_b (M_{\odot})	M_{cut} (M_{\odot})	T_0 (GK)	$\text{Log}_{10}(\rho_0)$ $\rho_0(\text{gm cm}^{-3})$	Y_e	$M(^{44}\text{Ti})$ $\times 10^{-5} (M_{\odot})$	$M(^{56}\text{Ni})$ $\times 10^{-2} (M_{\odot})$	$\frac{M(^{44}\text{Ti})}{M(^{56}\text{Ni})}$ $\times 10^{-5}$
15	0.50	0.24	1.40	1.45	1.450				1.22	9.0	13.9
	0.50	0.24	1.40	1.45	1.500				0.43	5.0	8.14
	0.50	0.24	1.40	1.45	1.600	4.848–2.483	7.120–5.962	0.497–0.499	0.08	0.3	23.9
	1.32	1.13	1.40	1.45	1.450				1.19	16.0	7.17
	1.32	1.13	1.40	1.45	1.500				0.24	14.0	1.78
	1.32	1.13	1.40	1.45	1.600	5.522–2.763	7.106–5.967	0.497–0.499	0.21	6.0	3.71
18	0.50	0.07	1.46	1.45	1.450				1.10	14.0	8.02
	0.50	0.07	1.46	1.45	1.500				0.30	11.0	2.75
	0.50	0.07	1.46	1.45	1.622	5.252–1.877	7.111–5.573	0.497–0.499	0.17	1.0	10.9
	1.32	0.93	1.46	1.45	1.450				1.09	20.0	5.42
	1.32	0.93	1.46	1.45	1.500				0.32	17.0	1.85
	1.32	0.93	1.46	1.45	1.622	6.176–2.609	7.278–5.915	0.497–0.499	0.27	8.0	3.49
22	1.32	0.70	1.58	1.60	1.600				1.14	22.0	5.25
	1.32	0.70	1.58	1.60	1.650				0.48	20.0	2.35
	1.32	0.70	1.58	1.60	1.820	5.704–2.651	7.199–5.957	0.498–0.499	0.46	9.0	4.85
	3.50	2.99	1.58	1.60	1.600				2.35	32.0	7.29
	3.50	2.99	1.58	1.60	1.650				1.14	32.0	3.60
	3.50	2.99	1.58	1.60	1.820	6.950–2.979	7.440–5.940	0.498–0.499	1.00	20.0	4.90
25	3.50	2.79	1.61	1.60	1.600				10.6	34.0	31.0
	3.50	2.79	1.61	1.60	1.650				9.99	34.0	29.4
	3.50	2.79	1.61	1.60	1.814	6.675–1.250	7.360–4.813	0.498–0.499	9.88	25.0	39.0

Note. Fe_{core} is the mass of the iron core. T_0 , $\text{Log}_{10}(\rho_0)$, and Y_e represent corresponding values from M_4 to the mass coordinate with no oxygen-burning. All other properties are described in the text.

Fryer et al. (2018)

$$T(t) = T_0 \exp\left(-\frac{t}{3\tau}\right) \quad \rho(t) = \rho_0 \exp\left(-\frac{t}{\tau}\right). \quad (2)$$

The power-law profile is based on a constant-velocity (homologous) expansion (see e.g., Magkotsios et al. 2010; Fryer et al. 2018), where the temporal evolution of shock-heated material is described as

$$T(t) = \frac{T_0}{2t+1} \quad \rho(t) = \frac{\rho_0}{(2t+1)^3}. \quad (3)$$

To inform comparisons with prior postprocessing studies using these analytic trajectories, we separately fit the temperature and density evolution of each zone of our models using Equations (2) and (3). We found that the power-law profile provides a superior reproduction of our data. This is consistent with Fryer et al. (2018), who found the power-law describes their data particularly well once the shock-heated material drops out of nuclear statistical equilibrium (NSE).

Magkotsios et al. (2010) studied the trends for ^{44}Ti and ^{56}Ni production in the T_0 – ρ_0 plane for both exponential and power-law profiles. Figure 1 shows a color map of their ^{44}Ti production across the T_0 – ρ_0 phase space for the power-law profile (Equation (3)) with electron-fraction $Y_e = 0.498$, which is close to the average $Y_e = 0.498$ – 0.499 range that we observe across each of our progenitor stars. For each M_{prog} and E_{inj} used in our CCSN calculations, we determined T_0 and ρ_0 for each mass zone, including these as data points in Figure 1. The figure includes labels for the four regions identified by Magkotsios et al. (2010) that are characterized by specific nuclear burning patterns and govern the yield of ^{44}Ti . Region A

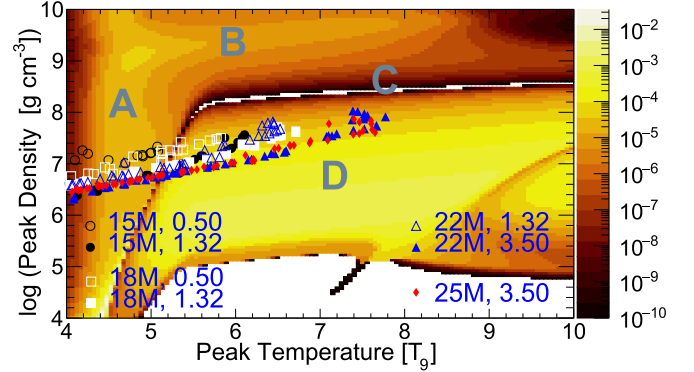


Figure 1. Peak temperature and peak density phase space traversed by radial mass zones in MESA for CCSN resulting from $M_{\text{prog}} = 15 M_{\odot}$, $18 M_{\odot}$, $22 M_{\odot}$, and $25 M_{\odot}$ models. As identified in Magkotsios et al. (2010), regions labeled in the plot are defined as A: Si-rich, B: Normal, C: QSE leakage, and D: α -rich. The legend refers to M_{prog} , followed by E_{inj} in 10^{51} erg. The color map indicates the ^{44}Ti mass fraction $X(^{44}\text{Ti})$, as calculated for power-law trajectories with $Y_e = 0.498$ by Magkotsios et al. (2010).

corresponds to incomplete silicon burning. Region B corresponds to normal freeze-out from NSE, where the abundance is largely determined from the Q -values of the reactions (Woosley et al. 1973; Meyer 1994; The et al. 1998; Hix & Thielemann 1999). Region C corresponds to the chasm region, where nucleosynthesis is characterized by the flow of material from a low- A quasistatic equilibrium (QSE) cluster containing ^{44}Ti to a high- A cluster containing ^{56}Ni . Region D corresponds to the α -rich freeze-out (Woosley et al. 1973).

Magkotsios et al. (2010) demonstrated that the yield of ^{44}Ti in shock-driven nucleosynthesis depends sensitively on the

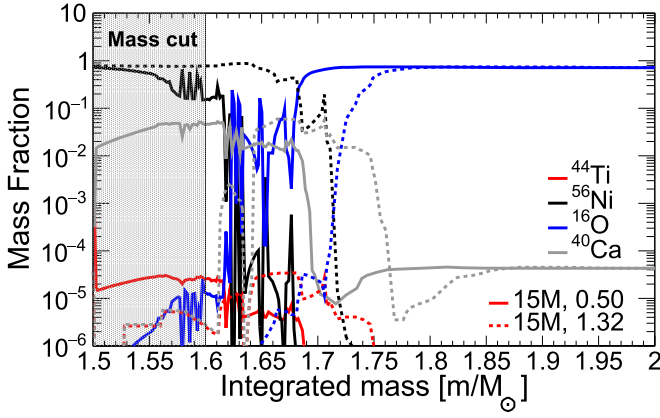


Figure 2. Mass fraction vs. integrated mass for various isotopes 5 s after the deposition of E_{inj} for calculations with $M_{\text{prog}} = 15 M_{\odot}$. E_{inj} is indicated by the line type: 0.50 foe (solid) and 1.32 foe (dotted).

location in the T_0 - ρ_0 plane and the expansion profile followed by the shock-heated material. The reaction rate sensitivities reported by that work were therefore specified by phase space region and expansion profile, including the impact on the topology of the phase space (e.g., chasm widening). Figure 1 shows that our $M_{\text{prog}} = 15 M_{\odot}$ $E_{\text{inj}} = 0.5$ foe model is limited to lower values of T_0 and does not cross the chasm region (Region C), while any other combination of E_{inj} with progenitor mass M_{prog} extends to higher T_0 and ρ_0 , into the α -rich freeze-out (Region D). The increase in maximum T_0 and ρ_0 with increasing M_{prog} and E_{inj} is also apparent.

4. Yields of ^{44}Ti and ^{56}Ni from Baseline Calculations

Prior to discussing the impact of varied nuclear reaction rates on ^{44}Ti and ^{56}Ni production, we first present results from our calculations using the baseline reaction rate library. The yields presented in Table 1 were determined by integrating the total mass of ^{44}Ti or ^{56}Ni outward from a lower-bound in mass known as the mass cut M_{cut} (Diehl & Timmes 1998). To help assess the impact of this arbitrary boundary on our results, we explored three choices of M_{cut} : I_b , $I_b + \Delta M_{\text{shell}}$, and M_4 . The latter is defined as the mass zone where entropy per nucleon $s = 4$, beyond which higher-dimensional models have found most material avoids fallback onto the protoneutron star (Ertl et al. 2016). In order to compare with postprocessing calculations, we determine $X(^{44}\text{Ti})$ and $X(^{56}\text{Ni})$ over the region between M_{cut} and the mass coordinate where there is no longer oxygen-burning, determining the mass-fraction per zone and taking an average weighted by the mass of each zone.

Figure 2 shows selected mass fractions following shock-driven nucleosynthesis for example calculations, with one value of M_{cut} shown for context. Clearly the choice of M_{cut} and E_{inj} will significantly affect yields of ^{44}Ti and ^{56}Ni , highlighting the need to explore nuclear sensitivities for multiple scenarios.

Figure 3 compares yields of ^{44}Ti and ^{56}Ni from our baseline calculations using various combinations of M_{prog} , E_{inj} , and M_{cut} to yields from model calculations of earlier studies, as well as inferred yields from astronomical observations. The boundary for observations of 1987A is based on the results of Boggs et al. (2015) ($M(^{44}\text{Ti}) = (1.5 \pm 0.3) \times 10^{-4} M_{\odot}$), Jerkstrand et al. (2011) ($M(^{44}\text{Ti}) = (1.5 \pm 0.5) \times 10^{-4} M_{\odot}$), Grebenev et al. (2012)

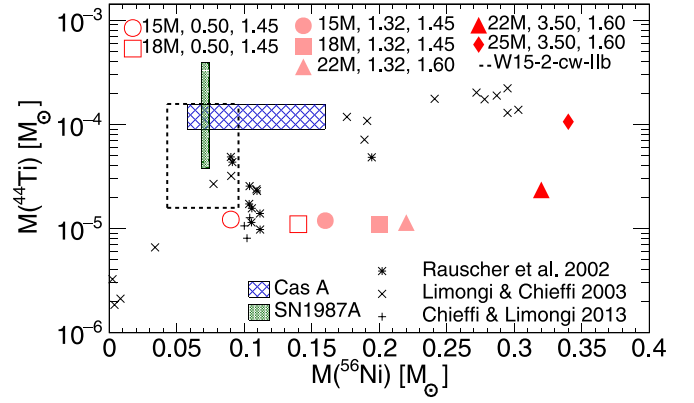


Figure 3. Total mass of ^{44}Ti and ^{56}Ni outside of $M_{\text{cut}} = I_b$ from our calculations, where the legend indicates M_{prog} , E_{inj} , M_{cut} . Results from previous observational and modeling work is shown for context. See the text for details.

($M(^{44}\text{Ti}) = (3.1 \pm 0.8) \times 10^{-4} M_{\odot}$), and Seitenzahl et al. (2014) ($M(^{44}\text{Ti}) = (0.55 \pm 0.17) \times 10^{-4} M_{\odot}$, $M(^{56}\text{Ni}) = (7.1 \pm 0.3) \times 10^{-2} M_{\odot}$). The boundary for observations of CasA is from Wang & Li (2016) ($M(^{44}\text{Ti}) = (1.3 \pm 0.4) \times 10^{-4} M_{\odot}$), Siegert et al. (2015) ($M(^{44}\text{Ti}) = (1.37 \pm 0.19) \times 10^{-4} M_{\odot}$), Grefenstette et al. (2014) ($M(^{44}\text{Ti}) = (1.25 \pm 0.3) \times 10^{-4} M_{\odot}$), and Eriksen et al. (2009) ($M(^{56}\text{Ni}) = 5.8\text{--}16.0 \times 10^{-2} M_{\odot}$). The boundary labeled W15-2-cw-1lb is from the 3D model calculation of Wongwathanarat et al. (2017) that resembled CasA. We note that comparisons to CasA may not be particularly relevant for this work, as this supernova is suspected to have originated from a progenitor that lost much of its hydrogen envelope (Koo et al. 2020). Results from 1D model calculations of Rauscher et al. (2002), Limongi & Chieffi (2003), and Chieffi & Limongi (2013) are also shown for $M_{\text{prog}} = 15\text{--}25 M_{\odot}$. While our ^{56}Ni yields are similar to these previous 1D calculations, our ^{44}Ti yields are generally lower, especially for our 18 and 22 M_{\odot} progenitors. This is likely due to the different explosion mechanism (the other works do not employ a thermal bomb) and our choice of E_{inj} and t_{inj} (Young & Fryer 2007; Fryer et al. 2012, 2018), but a more comprehensive cross-model comparison, which is beyond the scope of the present work, would be necessary to comment further.

To provide further context for comparisons to earlier 1D modeling work, we calculate the explosion energy E_{exp} as described by Aufderheide et al. (1991) and restated in Equations (4) and (5):

$$E_{\text{exp}} = E_{\text{inj}} + E_b + \Delta E_n, \quad (4)$$

where

$$E_b = E_k - E_{\text{Gv}} + E_{\text{int}}. \quad (5)$$

Here E_k is the total kinetic energy, E_{Gv} is the total gravitational energy, E_{int} is the total internal energy, E_b is the total binding energy, and ΔE_n is the nuclear binding energy released by burning. All the energy values are calculated from I_b to the surface of a star. Compared to previous works (e.g., Aufderheide et al. 1991; Rauscher et al. 2002; Limongi & Chieffi 2003), our calculations with the lower of two E_{inj} for a given M_{prog} result in relatively low E_{exp} , though the high E_{inj} $M_{\text{prog}} = 22 M_{\odot}$ and $25 M_{\odot}$ cases result in relatively high E_{exp} .

Table 2
Reaction Rate Variation Factors (RR)

$(\alpha, n), (n, \alpha)$			$(\alpha, p), (p, \alpha)$			(p, γ)		
Reactions	RR (↑)(↓)	Reac #	Reactions	RR (↑)(↓)	Reac #	Reactions	RR (↑)(↓)	Reac #
$^{10}\text{B}(\alpha, n)^{13}\text{N}$	20% (1)	1	$^{44}\text{Ti}(\alpha, p)^{47}\text{V}$	44% (10) ^a	7	$^{45}\text{V}(p, \gamma)^{46}\text{Cr}$	10	33
$^{11}\text{B}(\alpha, n)^{14}\text{N}$	10% (2)	2	$^{40}\text{Ca}(\alpha, p)^{43}\text{Sc}$	15% (11)	8	$^{41}\text{Sc}(p, \gamma)^{42}\text{Ti}$	100	34
$^{23}\text{Mg}(n, \alpha)^{20}\text{Ne}$	100	3	$^{17}\text{F}(\alpha, p)^{20}\text{Ne}$	100	9	$^{43}\text{Sc}(p, \gamma)^{44}\text{Ti}$	10	35
$^9\text{Be}(\alpha, n)^{12}\text{C}$	10% (3)	4	$^{21}\text{Na}(\alpha, p)^{24}\text{Mg}$	100	10	$^{44}\text{Ti}(p, \gamma)^{45}\text{V}$	100	36
$^{42}\text{Ca}(\alpha, n)^{45}\text{Ti}$	21% (4)	5	$^{27}\text{Al}(\alpha, p)^{30}\text{Si}$	100	11	$^{57}\text{Ni}(p, \gamma)^{58}\text{Cu}$	10	37
$^{34}\text{S}(\alpha, n)^{37}\text{Ar}$	16% (5)	6	$^{55}\text{Co}(\alpha, p)^{58}\text{Ni}$	10	12	$^{40}\text{Ca}(p, \gamma)^{41}\text{Sc}$	100	38
$^{27}\text{Al}(\alpha, n)^{30}\text{P}$	10	50	$^{48}\text{Cr}(\alpha, p)^{51}\text{Mn}$	100	13	$^{44}\text{V}(p, \gamma)^{45}\text{Cr}$	100	39
(α, γ)			$^{52}\text{Fe}(\alpha, p)^{55}\text{Co}$	100	14	$^{43}\text{Ti}(p, \gamma)^{44}\text{V}$	10	40
Reactions	RR (↑)(↓)	Reac #	$^{54}\text{Fe}(\alpha, p)^{57}\text{Co}$	8% (12)	15	$^{42}\text{Sc}(p, \gamma)^{43}\text{Ti}$	10	41
$^{40}\text{Ca}(\alpha, \gamma)^{44}\text{Ti}$	25% (6)	24	$^{56}\text{Ni}(\alpha, p)^{59}\text{Cu}$	10	16	$^{57}\text{Cu}(p, \gamma)^{58}\text{Zn}$	100	42
$^{12}\text{C}(\alpha, \gamma)^{16}\text{O}$	20% (7)(8)	25	$^6\text{Li}(\alpha, p)^9\text{Be}$	100	17	$^{20}\text{Ne}(p, \gamma)^{21}\text{Na}$	12% (15) ^b	43
$^7\text{Be}(\alpha, \gamma)^{11}\text{C}$	100	26	$^{13}\text{N}(\alpha, p)^{16}\text{O}$	100	18	$^{47}\text{V}(p, \gamma)^{48}\text{Cr}$	10	44
$^{24}\text{Mg}(\alpha, \gamma)^{28}\text{Si}$	10 ^c	27	$^{42}\text{Ca}(\alpha, p)^{45}\text{Sc}$	21% (13)	19	$^{42}\text{Ca}(p, \gamma)^{43}\text{Sc}$	21% (16)	45
$^{42}\text{Ca}(\alpha, \gamma)^{46}\text{Ti}$	15% (9)	28	$^{43}\text{Sc}(\alpha, p)^{46}\text{Ti}$	10	20	$^{39}\text{K}(p, \gamma)^{40}\text{Ca}$	100 ^d	46
$(p, n), (n, p)$			$^{58}\text{Ni}(\alpha, p)^{61}\text{Cu}$	25% (14)	21	$^{57}\text{Co}(p, \gamma)^{58}\text{Ni}$	10	47
Reactions	RR (↑)(↓)	Reac #	$^{38}\text{Ca}(\alpha, p)^{41}\text{Sc}$	100	22	$^{54}\text{Fe}(p, \gamma)^{55}\text{Co}$	12% (17)	48
$^{57}\text{Ni}(n, p)^{57}\text{Co}$	100	29	$^{34}\text{Ar}(\alpha, p)^{37}\text{K}$	100	23	$^{52}\text{Mn}(p, \gamma)^{53}\text{Fe}$	10	49
$^{56}\text{Co}(p, n)^{56}\text{Ni}$	100	30	$^{39}\text{K}(p, \alpha)^{36}\text{Ar}$	100	51			
$^{27}\text{Si}(n, p)^{27}\text{Al}$	100	31						
$^{11}\text{C}(n, p)^{11}\text{B}$	100	32						

Notes. The rate numbers are used as identifiers in Figures 4–6.

^a Subsequent evaluations (Hoffman et al. 2010; K. Chipps et al. 2020, in preparation) suggest that Sonzogni et al. (2000) underestimate the rate uncertainty and that a factor of 3 or more would be more appropriate.

^b Lyons et al. (2018) have since updated the rate, but the rate and uncertainty are similar in our temperature range of interest.

^c The evaluation of Adsley et al. (2020) suggests a much smaller factor may be appropriate; however, they focused on lower temperatures than are of interest for this work.

^d Our calculations were performed prior to the rate evaluation of Longland et al. (2018), who suggest $\sim \times 10$ is likely a more appropriate factor for the temperature range of interest. However, we note that experimental coverage is incomplete for the relevant center of mass energies.

References. (1) Gibbons & Macklin (1959), (2) Wang et al. (1991), (3) Wrean et al. (1994), (4) Cheng & King (1979), (5) Scott et al. (1993), (6) Robertson et al. (2012), (7) Plag et al. (2012), (8) deBoer et al. (2017), (9) Mitchell et al. (1985), (10) Sonzogni et al. (2000), (11) Howard et al. (1974), (12) Tims et al. (1991), (13) Buckby & King (1983), (14) Vlieks et al. (1974), (15) Rolfs et al. (1975), (16) Vlieks et al. (1978), (17) Kennett et al. (1981).

5. Reaction Rate Variations

For each combination of M_{prog} and E_{inj} listed in Table 1, we performed reaction rate variations and assessed the change in ^{44}Ti and ^{56}Ni yields relative to the baseline calculation. Given the computational expense, we chose to vary a single reaction rate at a time, as opposed to varying several rates at once in a Monte Carlo fashion (e.g., Bliss et al. 2020). We limited our investigation to the 49 reaction rates identified as high impact by Magkotsios et al. (2010), excluding the weak rates identified in that work, along with two additional reaction rates chosen to test the completeness of the 49-rate list. The reaction list, given in Table 2, includes the additional two reactions $^{27}\text{Al}(\alpha, n)^{30}\text{P}$ and $^{39}\text{K}(p, \alpha)^{36}\text{Ar}$ based on suspected impact due to the reaction network flow (see Figure 7).

Similar past studies have often adopted reaction rate variation factors $\times 100$ and $/100$ (e.g., The et al. 1998; Magkotsios et al. 2010), since these studies aimed to find all plausible sensitivities. However, concerted efforts from the nuclear physics community have reduced the uncertainties for several reaction rates well below two orders of magnitude uncertainty. Furthermore, decades of comparison between

measured data and Hauser–Feshbach calculations have shown that nuclear reactions proceeding through compound nuclei at relatively high nuclear level densities have theoretical predictions generally within an order of magnitude of measurements (see, e.g., Mohr 2015). As such, we aimed to adopt more realistic rate variation factors, taking into account existing experimental and theoretical data.

Reaction rate variation factors used here are given in Table 2. When experimental data were available over the astrophysically relevant energies or a reaction rate evaluation existed, the uncertainty from that work was used as the rate variation factor. In the absence of such information, the rate was either assigned an uncertainty factor of 10 or 100, depending on whether or not the Hauser–Feshbach formalism was thought to be valid, following the approach of Cyburt et al. (2016).

For Hauser–Feshbach validity, we adopt the heuristic that more than 10 nuclear levels must exist within an MeV of the excitation energy populated in the compound nucleus for a particular reaction (Wagoner 1969; Rauscher et al. 1997). To determine the relevant excitation energy, we use the Gamow

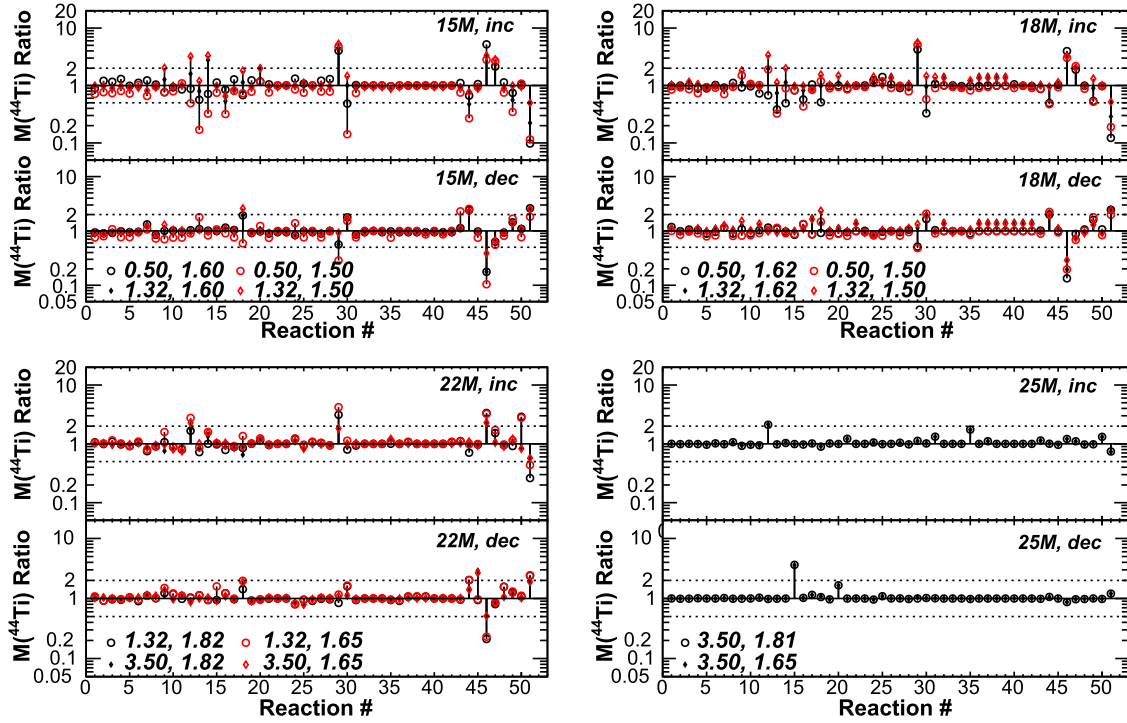


Figure 4. Ratio of $M(^{44}\text{Ti})$ to the baseline calculation results of Table 1 when varying each reaction of Table 2 by its uncertainty factor upward (upper panel) or downward (lower panel). The legends indicate E_{inj} , M_{cut} . The dashed lines demarcate factor of two impacts.

window approximation for the center of mass reaction energy of astrophysical interest (Rolfs & Rodney 1988):

$$E_G = 0.1220 \left(Z_1^2 Z_2^2 \frac{A_1 A_2}{(A_1 + A_2)} T_9^2 \right)^{1/3} \text{ MeV}, \quad (6)$$

where Z_i are the proton numbers of the two reactants, A_i are their mass numbers, T_9 is the environment temperature in gigakelvin, and k_B is the Boltzmann constant. The $1/e$ width of the window about E_G is

$$\Delta_G = 4 \sqrt{\left(\frac{E_G k_B T_9}{3} \right)} \text{ MeV}. \quad (7)$$

While more accurate methods exist to determine the excitation energy window of astrophysical interest (Newton et al. 2007; Rauscher 2010), we chose the more approximate Gamow window method given the uncertainty of nuclear level structure for the nuclides involved and the choice of a single temperature for which to calculate the energies of astrophysical interest.

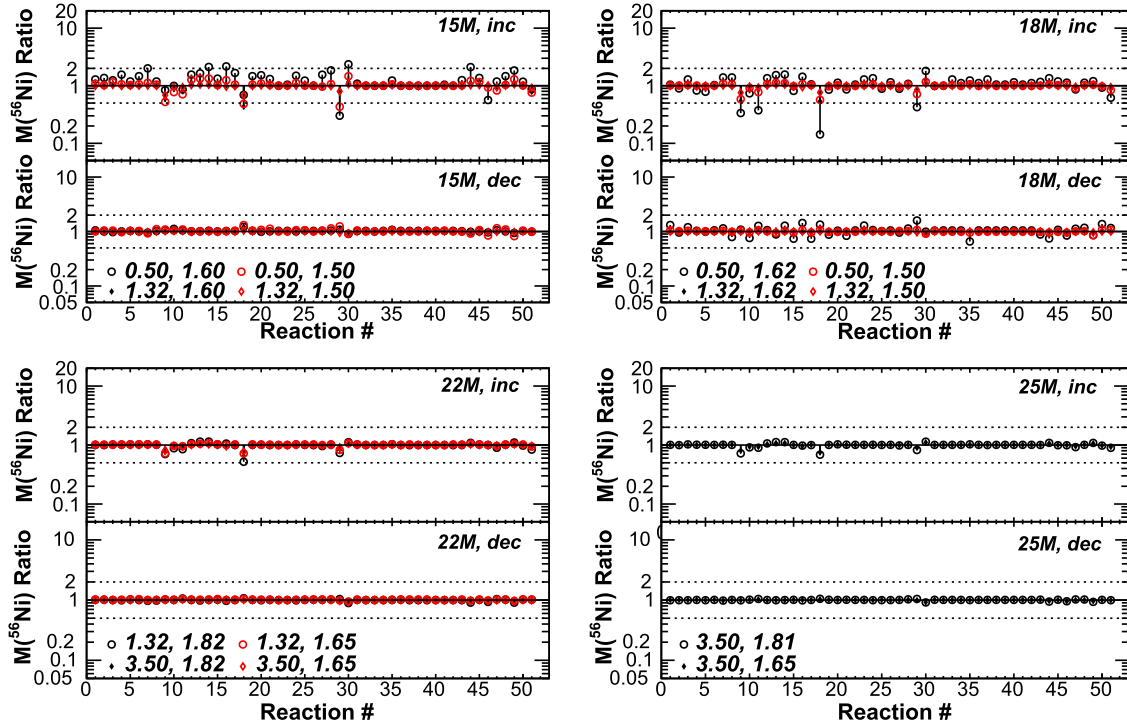
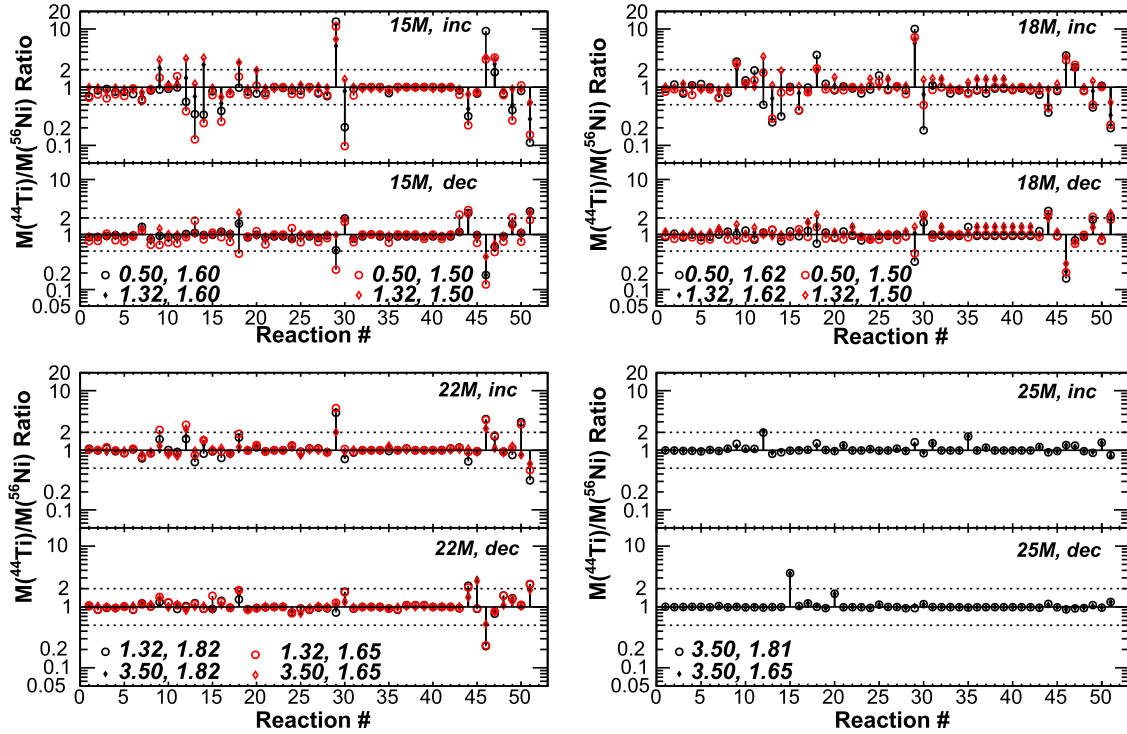
We calculated the Gamow window at $T_9 = 4$ as this is where the calculations of Magkotsios et al. (2010) fall out of QSE. We determined whether at the bottom of the window ($E_G - \Delta_G/2$) more than 10 nuclear levels per MeV of excitation were present, based on the microscopic nuclear level densities calculated by Goriely et al. (2008). For high level-density cases, we consider a reaction to be in the statistical regime and assign an uncertainty factor of 10, based on the typical spread in predictions from Hauser-Feshbach calculations (e.g., Pereira & Montes 2016). For low level-density cases, we consider a reaction to be in the resonant regime and assign an uncertainty factor of 100, based on the significant rate modification that can occur due to addition/removal of a particular resonance or change in a key resonance’s properties (e.g., Cavanna et al. 2015).

6. Sensitivity Study Results

Figures 4–6 show the sensitivity study results for ^{44}Ti , ^{56}Ni , and $^{44}\text{Ti}/^{56}\text{Ni}$, respectively, for all combinations of M_{prog} , E_{inj} , and M_{cut} modeled here, where the reaction numbers correspond to the designations in Table 2 and the reported ratios are to the baseline results of Table 1. In each plot the upper panel corresponds to a reaction rate increase, while the bottom panel corresponds to a reaction rate decrease. We show the sensitivities for various combinations of E_{inj} and M_{cut} to give a sense of the robustness of our results to changes in model assumptions. However, for the ensuing discussion we limit ourselves to the results for $M_{\text{cut}} = M_4$.

In the following, we separately discuss reactions impacting ^{44}Ti , ^{56}Ni , and their ratio. Motivated by typical observational uncertainties (discussed in Section 4), we only discuss cases (listed in Table 3) that affect these yields by a factor of two or more for at least one set of model conditions, as we deem this to be significant for model-observation comparisons. Of course as observations improve, it is likely that even smaller sensitivities will be of interest in the future. Note that in general we see fewer reaction rate variations having a significant impact for larger M_{prog} calculations. This is because, for those cases, much of the ^{44}Ti and ^{56}Ni beyond M_{cut} was synthesized during stellar evolution at radii not significantly impacted by the outgoing shock (Chieffi & Limongi 2017).

The explanations we provide for the sensitivities we observe are based on analyzing the flow in the nuclear reaction network (see Figure 7), along with guidance from the discussions in The et al. (1998) and Magkotsios et al. (2010). The flow for converting isotope i to isotope j over a timestep is $\mathcal{F}_{ij} = \int (\dot{Y}_{i \rightarrow j} - \dot{Y}_{j \rightarrow i}) dt$, where $\dot{Y}_{i \rightarrow j}$ is the rate that the abundance of isotope i is depleted by reactions converting i to j . As shown in Figure 1, the relevant conditions for this work are primarily those known as α -rich and silicon-rich freeze-out.

Figure 5. Same as Figure 4, but for $M(^{56}\text{Ni})$.Figure 6. Same as Figure 4, but for $M(^{44}\text{Ti})/M(^{56}\text{Ni})$.

For silicon-rich conditions (Region A), nucleosynthesis yields are mostly characterized by nuclear masses and the initial abundances before the explosion, with some flow between many small QSE clusters. For α -rich freeze-out (Region D), much larger QSE clusters are formed initially and a significant excess of α -particles are available. In that case nucleosynthesis is characterized by the flow between these large QSE clusters

and the fusion of α -particles into heavier nuclides with $Z = 2n$, $A = 4n$, where n is an integer. Therefore, our reaction rate sensitivities fall into three categories: those influencing the helium burning, those near boundaries of the large QSE clusters that exist in α -rich freeze-out at early times, and those near ^{44}Ti that can influence nucleosynthesis as that QSE cluster dissolves into many smaller QSE clusters.

Table 3
Ratios to the $M_{\text{cut}} = M_4$ Baseline Calculation Results of Table 1 for Reaction Rates Significantly Impacting $M(^{44}\text{Ti})$, $M(^{56}\text{Ni})$, and/or $M(^{44}\text{Ti})/M(^{56}\text{Ni})$

Reactions	RR	$M(^{44}\text{Ti})/M(^{44}\text{Ti}) _{\text{baseline}}$								$M(^{56}\text{Ni})/M(^{56}\text{Ni}) _{\text{baseline}}$								$[M(^{44}\text{Ti})/M(^{56}\text{Ni})]/[M(^{44}\text{Ti})/M(^{56}\text{Ni})] _{\text{baseline}}$							
		15 M_{\odot}		18 M_{\odot}		22 M_{\odot}		25 M_{\odot}	15 M_{\odot}		18 M_{\odot}		22 M_{\odot}		25 M_{\odot}	15 M_{\odot}		18 M_{\odot}		22 M_{\odot}		25 M_{\odot}			
		0.5	1.32	0.5	1.32	1.32	3.5		0.5	1.32	0.5	1.32	1.32	3.5		0.5	1.32	0.5	1.32	1.32	3.5				
$^{17}\text{F}(\alpha, p)^{20}\text{Ne}$	$\times 100$	0.8	1.3	0.9	1.1	1.1	0.8	0.9	0.8	0.6	0.3	0.5	0.7	0.8	0.7	0.9	2.1	2.8	2.1	1.5	1.0	1.3			
	$\times 0.01$	1.2	1.0	1.1	1.3	1.2	1.3	1.0	1.4	1.1	1.1	1.0	1.0	1.0	1.0	0.8	1.0	1.0	1.2	1.2	1.3	1			
$^{27}\text{Al}(\alpha, p)^{30}\text{Si}$	$\times 100$	0.8	1.0	0.7	1.0	0.8	0.8	0.9	0.9	0.8	0.4	0.8	0.8	0.9	0.9	1.0	1.2	1.9	1.2	0.9	0.9	1.0			
	$\times 0.01$	1.2	1.0	1.0	1.2	1.0	1.1	1.0	1.6	1.0	1.3	1.1	1.1	1.0	1.0	0.8	0.9	0.9	1.1	0.9	1.0	1.0			
$^{55}\text{Co}(\alpha, p)^{58}\text{Ni}$	$\times 10$	0.9	1.6	0.7	2.0	1.7	1.8	2.1	1.6	1.1	1.4	1.1	1.1	1.0	1.1	0.6	1.4	0.5	1.8	1.5	1.7	2.0			
	$\times 0.1$	1.3	1.0	1.2	1.1	1.0	0.9	1.0	1.3	1.0	1.1	1.0	1.0	1.0	1.0	1.0	1.0	1.1	1.1	1.0	0.9	1.0			
$^{48}\text{Cr}(\alpha, p)^{51}\text{Mn}$	$\times 100$	0.6	0.8	0.4	0.7	0.7	0.9	1.0	1.6	1.2	1.5	1.2	1.1	1.1	1.1	0.3	0.7	0.2	0.6	0.6	0.8	0.9			
	$\times 0.01$	1.2	1.1	1.1	1.0	1.1	1.0	1.0	1.4	1.0	0.9	1.0	1.0	1.0	1.0	0.9	1.1	1.2	1.0	1.2	1.0	1.0			
$^{52}\text{Fe}(\alpha, p)^{55}\text{Co}$	$\times 100$	0.7	2.8	0.5	1.1	1.0	1.3	1.0	2.1	1.1	1.6	1.2	1.1	1.1	1.1	0.3	2.4	0.3	1.0	0.9	1.2	0.9			
	$\times 0.01$	1.2	1.0	1.0	1.0	0.9	1.1	1.0	1.3	1.0	1.3	1.0	1.0	1.0	1.0	0.9	1.0	0.8	1.0	0.9	1.1	1.0			
$^{54}\text{Fe}(\alpha, p)^{57}\text{Co}$	$\times 1.08$	1.1	1.0	0.8	1.0	1.0	1.1	1.0	1.3	1.0	0.8	1.0	1.0	1.0	1.0	0.8	1.0	1.0	0.9	1.0	1.1	1.0			
	$\times 0.92$	1.1	1.0	0.8	1.0	0.9	0.9	3.6	1.2	1.0	0.7	1.0	1.0	1.0	1.0	0.9	1.0	1.2	1.0	1.0	1.0	3.6			
$^{56}\text{Ni}(\alpha, p)^{59}\text{Cu}$	$\times 10$	0.8	0.5	0.6	0.8	0.8	1.0	1.0	2.2	1.0	1.4	1.0	1.1	1.0	1.0	0.4	0.5	0.4	0.8	0.7	1.0	1.0			
	$\times 0.1$	1.2	1.1	1.3	1.2	1.2	1.1	1.0	1.5	1.0	1.4	1.0	1.0	1.0	1.0	0.8	1.1	0.9	1.2	1.3	1.1	1.0			
$^{13}\text{N}(\alpha, p)^{16}\text{O}$	$\times 100$	0.8	1.1	0.5	1.0	0.8	0.6	0.9	0.7	0.4	0.1	0.5	0.5	0.6	0.7	1.0	2.6	3.6	1.8	1.6	1.0	1.3			
	$\times 0.01$	1.3	1.9	0.9	1.4	1.4	1.6	1.1	1.7	1.2	1.3	1.0	1.1	1.0	1.0	0.8	1.6	0.7	1.4	1.3	1.6	1.0			
$^{43}\text{Sc}(\alpha, p)^{46}\text{Ti}$	$\times 10$	1.2	2.1	1.0	1.1	1.1	1.2	1.0	1.5	1.1	1.1	1.0	1.0	1.0	1.0	0.8	1.9	0.9	1.1	1.1	1.2	1.0			
	$\times 0.1$	1.1	1.0	0.9	1.2	1.0	1.0	1.7	1.4	1.0	1.0	1.0	1.0	1.0	1.0	0.8	1.0	0.9	1.2	1.0	1.0	1.6			
$^{57}\text{Ni}(n, p)^{57}\text{Co}$	$\times 100$	4.0	4.2	4.2	4.8	3.1	1.8	1.1	0.3	0.8	0.4	0.8	0.7	0.9	0.8	13.4	5.1	10.0	5.7	4.3	2.1	1.4			
	$\times 0.01$	0.7	0.6	0.5	1.1	0.8	1.0	1.0	1.8	1.1	1.6	1.1	1.0	1.0	1.0	0.4	0.5	0.3	1.1	0.8	1.0	1.0			
$^{56}\text{Co}(p, n)^{56}\text{Ni}$	$\times 100$	0.5	1.0	0.3	1.0	0.8	0.9	1.0	2.4	1.2	1.8	1.3	1.1	1.1	1.1	0.2	0.8	0.2	0.8	0.7	0.8	0.9			
	$\times 0.01$	1.6	1.8	1.6	2.0	1.6	1.2	1.0	1.2	0.9	1.0	0.9	0.9	0.9	0.9	1.4	2.0	1.7	2.3	1.8	1.3	1.1			
$^{47}\text{V}(p, \gamma)^{48}\text{Cr}$	$\times 10$	0.7	0.5	0.5	0.5	0.7	0.9	1.0	2.1	1.1	1.4	1.1	1.1	1.0	1.1	0.3	0.4	0.4	0.5	0.6	0.9	0.9			
	$\times 0.1$	2.0	2.4	2.0	2.2	2.0	1.5	1.1	1.0	1.0	0.7	1.0	0.9	1.0	0.9	2.2	2.5	2.7	2.3	2.2	1.6	1.1			
$^{42}\text{Ca}(p, \gamma)^{43}\text{Sc}$	$\times 1.21$	1.1	0.9	1.0	1.0	1.0	0.9	1.0	1.4	1.1	1.2	1.0	1.0	1.0	1.0	0.8	0.8	0.9	1.0	1.0	0.9	1.0			
	$\times 0.79$	1.1	1.0	1.0	1.1	0.9	2.9	1.0	1.2	1.0	1.1	1.0	1.0	1.0	1.0	0.9	1.0	0.9	1.2	0.9	2.9	1.0			
$^{39}\text{K}(p, \gamma)^{40}\text{Ca}$	$\times 100$	5.2	3.5	4.0	3.5	3.4	2.4	1.2	0.6	1.0	1.1	1.0	1.0	1.0	1.0	9.2	3.5	3.5	3.4	3.3	2.4	1.2			
	$\times 0.01$	0.1	0.2	0.1	0.2	0.2	0.5	0.9	1.1	1.0	0.8	0.9	0.9	1.0	1.0	0.1	0.2	0.2	0.2	0.2	0.5	0.9			
$^{57}\text{Co}(p, \gamma)^{58}\text{Ni}$	$\times 10$	2.1	2.3	1.9	2.0	1.5	1.1	1.1	1.2	0.9	0.9	0.9	0.9	1.0	0.9	1.8	2.5	2.2	2.2	1.7	1.2	1.2			
	$\times 0.1$	1.2	0.6	0.9	0.8	0.8	0.8	1.0	1.9	1.1	1.1	1.0	1.0	1.0	1.0	0.6	0.6	0.8	0.7	0.8	0.8	0.9			
$^{52}\text{Mn}(p, \gamma)^{53}\text{Fe}$	$\times 10$	0.7	0.6	0.5	0.9	0.9	1.1	1.0	1.8	1.1	1.2	1.0	1.1	1.0	1.1	0.4	0.5	0.5	0.9	0.8	1.0	0.9			
	$\times 0.1$	1.5	1.4	1.6	1.4	1.3	1.3	1.0	0.9	0.9	0.9	0.9	0.9	0.9	0.9	1.6	1.5	1.9	1.5	1.4	1.4	1.1			
$^{27}\text{Al}(\alpha, n)^{30}\text{P}$	$\times 10$	1.0	1.0	1.0	1.0	2.9	0.9	1.3	1.2	1.0	0.9	1.0	1.0	1.0	1.0	0.9	1.0	1.1	1.0	3.0	0.9	1.4			
	$\times 0.1$	1.2	1.1	1.1	0.9	1.1	1.0	1.0	1.2	1.0	1.4	1.0	1.0	1.0	1.0	1.0	1.1	0.8	0.9	1.1	1.0	1.0			

 ∞

Table 3
(Continued)

Reactions	RR	$M(^{44}\text{Ti})/M(^{44}\text{Ti}) _{\text{baseline}}$								$M(^{56}\text{Ni})/M(^{56}\text{Ni}) _{\text{baseline}}$								$[M(^{44}\text{Ti})/M(^{56}\text{Ni})]/[M(^{44}\text{Ti})/M(^{56}\text{Ni})] _{\text{baseline}}$							
		$15 M_{\odot}$		$18 M_{\odot}$		$22 M_{\odot}$		$25 M_{\odot}$		$15 M_{\odot}$		$18 M_{\odot}$		$22 M_{\odot}$		$25 M_{\odot}$		$15 M_{\odot}$		$18 M_{\odot}$		$22 M_{\odot}$		$25 M_{\odot}$	
		0.5	1.32	0.5	1.32	1.32	3.5	3.5		0.5	1.32	0.5	1.32	1.32	3.5	3.5		0.5	1.32	0.5	1.32	1.32	3.5	3.5	
$^{39}\text{K}(p, \alpha)^{36}\text{Ar}$	$\times 100$	0.1	0.2	0.1	0.3	0.3	0.6	0.7		0.9	0.8	0.6	0.9	0.8	0.9	0.9		0.1	0.3	0.2	0.3	0.3	0.6	0.8	
	$\times 0.01$	3.3	2.6	2.4	2.6	2.4	2.0	1.2		1.0	1.0	1.2	1.0	1.0	1.0	1.0		3.4	2.6	2.1	2.6	2.4	2.0	1.2	

Note. Ratios greater than a factor of two increase or reduction are bolded for readability. The RR column lists the reaction rate multiplication factor. Subcolumns under each M_{prog} indicate E_{inj} in foe.

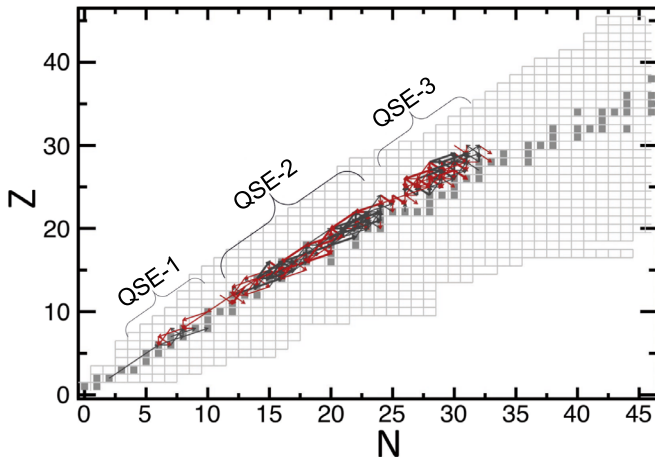


Figure 7. Reaction network flow for $M_{\text{prog}} = 15 M_{\odot}$ with $E_{\text{inj}} = 1.32$ for 0.06 s after the completion of energy deposition. Forward reaction rate flow is shown by black arrows, while the red arrows represent the reverse reaction flow. We refer to (p, γ) , (p, n) , (α, γ) , (α, p) , and (α, n) as forward. Three QSE regions that are present early in the calculation are identified in the reaction flow. Note that these begin as a single large QSE cluster and dissolve into many smaller QSE clusters.

6.1. Reactions Impacting ^{44}Ti

Here we discuss reactions listed in Table 3 that significantly impact $M(^{44}\text{Ti})$, working from light to heavy nuclides.

$^{13}\text{N}(\alpha, p)^{16}\text{O}$ and $^{27}\text{Al}(\alpha, n)^{30}\text{P}$ each influence $M(^{44}\text{Ti})$ for a subset of conditions, where a rate increase of the former reduces ^{44}Ti yields, while an increase of the latter increases $M(^{44}\text{Ti})$. Each is a prominent helium-burning reaction in our network flow. However, the lack of consistency in influence across M_{prog} and E_{inj} demonstrates a clear dependence on the adopted model conditions.

$^{39}\text{K}(p, \gamma)^{40}\text{Ca}$ and $^{39}\text{K}(p, \alpha)^{36}\text{Ar}$ significantly impact $M(^{44}\text{Ti})$ across almost all sets of model conditions. This is due to the importance of the reaction sequence $^{39}\text{K}(p, \gamma)^{40}\text{Ca}(\alpha, \gamma)^{44}\text{Ti}$. Increasing $^{39}\text{K}(p, \gamma)^{40}\text{Ca}$ clearly enhances $M(^{44}\text{Ti})$, whereas $^{39}\text{K}(p, \alpha)^{36}\text{Ar}$ competes as an alternative reaction path, reducing $M(^{44}\text{Ti})$. In each case, a reaction rate decrease has the opposite effect.

$^{42}\text{Ca}(p, \gamma)^{43}\text{Sc}$ is generally well constrained enough so as to not impact ^{44}Ti nucleosynthesis. However, for the $22 M_{\odot}$ high- E_{inj} case, decreasing this reaction rate significantly enhances $M(^{44}\text{Ti})$. The connection of ^{42}Ca to ^{44}Ti along the reaction network is not as straightforward as one might assume, since $^{43}\text{Sc}(\gamma, p)^{42}\text{Ca}$ dwarfs the forward reaction at the relevant temperatures. The influence of decreasing the $^{42}\text{Ca}(p, \gamma)^{43}\text{Sc}$ reaction rate is to reduce competition with $^{42}\text{Ca}(\alpha, n)^{45}\text{Ti}$. The latter reaction enhances $M(^{44}\text{Ti})$ since the abundances across titanium isotopes will be redistributed according to $(n, \gamma) - (\gamma, n)$ equilibrium until the environment has cooled and nucleosynthesis has essentially ceased.

An increase in the $^{43}\text{Sc}(\alpha, p)^{46}\text{Ti}$ rate was found to enhance $M(^{44}\text{Ti})$ only for the $15 M_{\odot}$ high- E_{inj} case, where the presumed connection to ^{44}Ti is as described in the previous paragraph for $^{42}\text{Ca}(\alpha, n)^{45}\text{Ti}$. Following the reaction network flow of Figure 7 also reveals the connection $^{43}\text{Sc}(\alpha, p)^{46}\text{Ti}(p, \gamma)^{47}\text{V}(p, \alpha)^{44}\text{Ti}$.

$^{47}\text{V}(p, \gamma)^{48}\text{Cr}$ significantly impacts $M(^{44}\text{Ti})$ for most of the model conditions explored. This reaction competes with $^{47}\text{V}(p, \alpha)^{44}\text{Ti}$, instead bridging the QSE leakage from QSE cluster 2 to QSE-3 (see Figure 7). Therefore, an increase in the

$^{47}\text{V}(p, \gamma)^{48}\text{Cr}$ rate decreases $M(^{44}\text{Ti})$, while a reaction rate decrease has the opposite effect.

$^{48}\text{Cr}(\alpha, p)^{51}\text{Mn}$ can be a part of the bridge connecting QSE-2 to QSE-3 and therefore an increase in this reaction rate decreases $M(^{44}\text{Ti})$ for low M_{prog} cases. However, when using the nominal $^{48}\text{Cr}(\alpha, p)^{51}\text{Mn}$ reaction rate, $^{48}\text{Cr}(n, p)^{48}\text{V}$ plays a more significant role bridging QSE-2 to QSE-3, and so a reaction rate decrease has little impact.

After the sequence $^{48}\text{V}(p, \gamma)^{49}\text{Cr}(p, n)^{49}\text{V}(p, \gamma)^{50}\text{Cr}(p, \gamma)^{51}\text{Mn}(n, p)^{51}\text{Cr}(p, \gamma)^{52}\text{Mn}$, $^{52}\text{Mn}(p, \gamma)^{53}\text{Fe}$ is near the upper end of the bridge between QSE-2 and QSE-3. As such, increasing this reaction rate decreases $M(^{44}\text{Ti})$, while decreasing the rate has the opposite effect, though our threshold for significance is only crossed for one set of model conditions.

The impact of $^{52}\text{Fe}(\alpha, p)^{55}\text{Co}$ significantly depends on the adopted model conditions, alternately enhancing or reducing $M(^{44}\text{Ti})$ from a reaction rate increase. In Region A, where the majority of the low- M_{prog} low- E_{inj} mass zones are located, ^{52}Fe is expected to be one of the primary freeze-out nuclides (Magkotsios et al. 2010), and so it is sensible that for these cases increasing the $^{52}\text{Fe}(\alpha, p)^{55}\text{Co}$ reaction rate will move the reaction network flow away from ^{44}Ti . However, for Region D, in which higher T_0 are experienced and (γ, p) reactions will play a more prominent role, enhancing $^{52}\text{Fe}(\alpha, p)^{55}\text{Co}$ ultimately leads to more significant flow toward ^{44}Ti . This case highlights the complexities of nuclear reaction network flows in high-temperature environments.

$^{54}\text{Fe}(\alpha, p)^{57}\text{Co}$ is quite well constrained experimentally and variations within the present uncertainty are largely inconsequential for ^{44}Ti nucleosynthesis. However, a decrease in this reaction rate significantly enhances $M(^{44}\text{Ti})$ for the highest M_{prog} calculation. This is likely due to the increased competition from the reaction sequence $^{54}\text{Fe}(p, \alpha)^{51}\text{Mn}(\gamma, p)^{50}\text{Cr}(p, \alpha)^{47}\text{V}(p, \alpha)^{44}\text{Ti}$.

As with $^{52}\text{Fe}(\alpha, p)^{55}\text{Co}$, the influence of $^{55}\text{Co}(\alpha, p)^{58}\text{Ni}$ on $M(^{44}\text{Ti})$ depends strongly on the model conditions, having the same relative influence as the former reaction for a reaction rate increase.

The majority of the remaining reactions on isotopes of cobalt and nickel influence $M(^{44}\text{Ti})$ as might be expected, with reactions moving toward ^{44}Ti enhancing its abundance and reactions moving away decreasing it. These include $^{56}\text{Co}(p, n)^{56}\text{Ni}$, $^{56}\text{Ni}(\alpha, p)^{59}\text{Cu}$, and $^{57}\text{Ni}(n, p)^{57}\text{Co}$. On the other hand, an increase of the $^{57}\text{Co}(p, \gamma)^{58}\text{Ni}$ reaction rate increases $M(^{44}\text{Ti})$. This somewhat counterintuitive result is apparently due to the flow connecting ^{58}Ni to ^{44}Ti via ^{54}Fe . Specifically, the reaction sequence $^{58}\text{Ni}(\gamma, n)^{57}\text{Ni}(\gamma, p)^{56}\text{Co}(\gamma, p)^{55}\text{Fe}(\gamma, n)^{54}\text{Fe}$ and onto ^{44}Ti as described in the preceding paragraph discussing $^{54}\text{Fe}(\alpha, p)^{57}\text{Co}$.

6.2. Reactions Impacting ^{56}Ni

Here we discuss the reactions listed in Table 3 that significantly impact $M(^{56}\text{Ni})$. As highlighted by Magkotsios et al. (2010), ^{56}Ni nucleosynthesis is far less sensitive to nuclear reaction rate variations than ^{44}Ti because it is much nearer to the global minimum in the nuclear binding energy surface. We find sensitivities for nuclear reaction rates impacting the flow into the large QSE cluster at early times and into the small QSE cluster present around ^{56}Ni at late times.

For α -rich freeze-out conditions, the $3\alpha \rightarrow ^{12}\text{C}$ reaction contributes flow to the single large QSE cluster that is initially present, driving the formation of the cluster QSE-1 (Magkotsios et al. 2010). $^{13}\text{N}(\alpha, p)^{16}\text{O}$, $^{17}\text{F}(\alpha, p)^{20}\text{Ne}$, and $^{27}\text{Al}(\alpha, p)^{30}\text{Si}$ all moderate flow from the QSE-1 cluster to higher-mass

nuclides. This has a significant impact on $M(^{56}\text{Ni})$ for a subset of our model calculations. For each of these reactions, an increase in the reaction rate decreases ^{56}Ni yields.

The $^{57}\text{Ni}(n, p)^{57}\text{Co}$ reaction drives material away from the nickel isotopes toward lower mass nuclides when the large QSE cluster in this region has dissolved. Therefore, increasing this reaction rate decreases $M(^{56}\text{Ni})$ for a subset of the model conditions.

6.3. Reactions Impacting $^{44}\text{Ti}/^{56}\text{Ni}$

Inspecting Table 3 reveals several reactions that impact $M(^{44}\text{Ti})$ and/or $M(^{56}\text{Ni})$ for some set of model conditions, but not above our pre-specified significance threshold. However, as the impacts on the two yields are often anticorrelated, two nonsignificant sensitivities can combine to form a significant impact on the ratio $M(^{44}\text{Ti})/M(^{56}\text{Ni})$. As this ratio is considered a distinct diagnostic for model-observation comparisons (e.g., Wongwathanarat et al. 2017), we separately highlight these reaction rate sensitivities in Table 3.

7. Discussion

It is interesting to compare the results of the present work to previous studies exploring nuclear reaction rate sensitivities of shock-driven nucleosynthesis. In particular, we focus our discussion on the postprocessing studies of The et al. (1998) and Magkotsios et al. (2010), as these studies also explored the impact of individual reaction rate variations for a large number of rates. The pioneering work of The et al. (1998) used an exponential temperature and density trajectory (see Equation (2)) with $T_0 = 5.5$ GK, $\rho_0 = 10^7$ g cm $^{-3}$, $Y_e = 0.497$, and 0.499 , and reaction rate variation factors of 100. Magkotsios et al. (2010) expanded on this work, exploring reaction rate sensitivities with rate variation factors of 100 for exponential and power-law trajectories (see Equation (3)), a large phase space of T_0 – ρ_0 (see Figure 1), and $Y_e = 0.48$ – 0.52 . In comparison, our model calculations have average $Y_e = 0.498$ – 0.499 , thermodynamic trajectories more closely resembling the power-law forms, with mass zones covering the T_0 – ρ_0 phase-space as shown in Figure 1, and focused mostly on the strong reactions identified as important by Magkotsios et al. (2010) using rate variation factors informed by the literature.

While our list of influential reactions shares several similarities with previous works, there are some conspicuous differences. In particular, we do not highlight many of the reactions that both prior studies identified as high-impact,⁵ namely, $^{40}\text{Ca}(\alpha, \gamma)^{44}\text{Ti}$, $^{44}\text{Ti}(\alpha, p)^{47}\text{V}$, $^{45}\text{V}(p, \gamma)^{46}\text{Cr}$, and $^{57}\text{Ni}(p, \gamma)^{58}\text{Cu}$. For each of these reactions, the likely explanation is that we used far smaller rate variation factors (see Table 2). For the first two in this set, this is based on the significant efforts in the nuclear physics community to reduce these reaction rate uncertainties. For the latter two, our reduced rate variation factors (10 as opposed to 100) are based on the presumed accuracy of Hauser–Feshbach reaction rate predictions given the high nuclear level densities involved.

Our relative insensitivity to variations in the $^{40}\text{Ca}(\alpha, \gamma)^{44}\text{Ti}$ and $^{44}\text{Ti}(\alpha, p)^{47}\text{V}$ rates when using experimentally constrained uncertainties⁶ is in agreement with Hoffman et al. (2010) who

sampled a slightly lower ρ_0 region of the thermodynamic phase space with models of CasA from Magkotsios et al. (2008). They found that remaining uncertainties in $^{40}\text{Ca}(\alpha, \gamma)^{44}\text{Ti}$ contribute a $\sim 20\%$ variation to $X(^{44}\text{Ti})$, while $^{44}\text{Ti}(\alpha, p)^{47}\text{V}$ uncertainties (estimated there as a factor of 3) lead to a 70% variation. Similarly, Tur et al. (2010) found the $3\alpha \rightarrow ^{12}\text{C}$ and $^{12}\text{C}(\alpha, \gamma)^{16}\text{O}$ reactions are sufficiently constrained from the standpoint of ^{44}Ti CCSN nucleosynthesis.

For the remaining high-impact cases of Magkotsios et al. (2010), the sensitivity identified in their work is for a region of phase space that our models did not populate. For $^{17}\text{F}(\alpha, p)^{20}\text{Ne}$, $^{21}\text{Na}(\alpha, p)^{24}\text{Mg}$, and $^{40}\text{Ca}(\alpha, p)^{43}\text{Sc}$, Magkotsios et al. (2010) only find a significant impact for relatively proton-rich initial conditions. For $^{41}\text{Sc}(p, \gamma)^{42}\text{Ti}$ and $^{44}\text{Ti}(p, \gamma)^{45}\text{V}$, Magkotsios et al. (2010) observe significant variations of $X(^{44}\text{Ti})$ only for quite high- T_0 low- ρ_0 conditions.

Indeed the significant reaction rate sensitivities that we identify in Table 2 are all highlighted as of secondary importance by Magkotsios et al. (2010). However, since their “secondary” designation is a general term for less than a factor of 10 variation in $X(^{44}\text{Ti})$ for any region within their full T_0 – ρ_0 phase space, a quantitative comparison is not possible. Qualitatively, we find a significant sensitivity in $M(^{44}\text{Ti})$ and/or $M(^{44}\text{Ti})/M(^{56}\text{Ni})$ for the majority of (α, p) and (p, γ) reactions identified by Magkotsios et al. (2010) as impacting the chasm depth, and a subset of the (p, n) reactions found to impact the chasm width. The connection of our results to the chasm are not surprising, as all of our model calculations have mass zones very near to or directly over this region.

Perhaps more interesting are the reaction rate sensitivities that we find in our work that were not identified by Magkotsios et al. (2010). We included $^{39}\text{K}(p, \alpha)^{36}\text{Ar}$ and $^{27}\text{Al}(\alpha, n)^{30}\text{P}$ as a test of the completeness of the previous survey, finding significant sensitivities for some choices of model conditions. This is not entirely unexpected, as The et al. (1998) identified $^{27}\text{Al}(\alpha, n)^{30}\text{P}$ and $^{36}\text{Ar}(\alpha, p)^{39}\text{K}$, the reverse of $^{39}\text{K}(p, \alpha)^{36}\text{Ar}$, as influential for some choices of Y_e . Nonetheless, this highlights the need for larger-scale reaction rate sensitivity studies for shock-driven nucleosynthesis using one-dimensional models.

8. Conclusions

We performed nuclear reaction rate sensitivity studies for ^{44}Ti and ^{56}Ni production in CCSN shock-driven nucleosynthesis using the code MESA. We evolved a range of M_{prog} stars to core collapse and induced an artificial explosion with a range of E_{inj} , analyzing nucleosynthesis yields for a range of M_{cut} , in order to gauge the robustness of our results to model calculation assumptions. For each set of model assumptions, we varied the strong reactions previously identified by Magkotsios et al. (2010) as influential for ^{44}Ti production, including two additional rates to test the completeness of the influential reaction rate set, using reaction rate variation factors based on uncertainty constraints in the literature.

We find a significant impact on ^{44}Ti and/or ^{56}Ni nucleosynthesis for only a subset of the influential reaction rates of Magkotsios et al. (2010), though this is likely attributable to the smaller reaction rate variation factors and different astrophysical conditions used in our work. Additionally, we find nucleosynthesis sensitivities for reaction rates not identified by Magkotsios et al. (2010). This indicates that larger-scale reaction rate sensitivity studies exploring an expanded set of reaction rates is desirable.

⁵ Here, we consider Table 4 of The et al. (1998) and reactions designated as “primary” in Table 3 of Magkotsios et al. (2010).

⁶ We performed test calculations using a rate variation factor of 100 for these two rates with $M_{\text{prog}} = 15 M_{\odot}$, $E_{\text{inj}} = 1.32$ foe, and found $M(^{44}\text{Ti})$ variations similar to Figure 14 of Magkotsios et al. (2010).

From the present work we conclude that additional effort is required from the nuclear physics community to reduced the reaction rate uncertainties for $^{13}\text{N}(\alpha, p)^{16}\text{O}$, $^{17}\text{F}(\alpha, p)^{20}\text{Ne}$, $^{27}\text{Al}(\alpha, p)^{30}\text{Si}$, $^{43}\text{Sc}(\alpha, p)^{46}\text{Ti}$, $^{48}\text{Cr}(\alpha, p)^{51}\text{Mn}$, $^{52}\text{Fe}(\alpha, p)^{55}\text{Co}$, $^{54}\text{Fe}(\alpha, p)^{57}\text{Co}$, $^{55}\text{Co}(\alpha, p)^{58}\text{Ni}$, $^{56}\text{Ni}(\alpha, p)^{59}\text{Cu}$, $^{57}\text{Ni}(n, p)^{57}\text{Co}$, $^{56}\text{Co}(p, n)^{56}\text{Ni}$, $^{39}\text{K}(p, \gamma)^{40}\text{Ca}$, $^{42}\text{Ca}(p, \gamma)^{43}\text{Sc}$, $^{47}\text{V}(p, \gamma)^{48}\text{Cr}$, $^{52}\text{Mn}(p, \gamma)^{53}\text{Fe}$, $^{57}\text{Co}(p, \gamma)^{58}\text{Ni}$, $^{27}\text{Al}(\alpha, n)^{30}\text{P}$, and $^{39}\text{K}(p, \alpha)^{36}\text{Ar}$.

We thank the Ohio Supercomputer Center for providing computational resources (Ohio Supercomputer Center 1987), R. Farmer for making his pre-supernova evolution inputs for MESA available and for assistance in their implementation, and F. X. Timmes for sharing the data from Magkotsios et al. (2010). This work was supported by the U.S. Department of Energy under grants DE-FG02-88ER40387 and DE-SC0019042, the National Nuclear Security Administration under grant DE-NA0003909, and has benefited from support by the National Science Foundation under grant PHY-1430152 (Joint Institute for Nuclear Astrophysics–Center for the Evolution of the Elements).

Software: Modules for Experiments in Stellar Astrophysics (MESA)(Paxton et al. 2011, 2013, 2015, 2018).

ORCID iDs

Shiv K. Subedi  <https://orcid.org/0000-0001-5898-1989>

Zach Meisel  <https://orcid.org/0000-0002-8403-8879>

References

- Adsley, P., Laird, A., & Meisel, Z. 2020, *PhRvC*, 102, 015801
- Aufderheide, M. B., Baron, E., & Thielemann, F.-K. 1991, *ApJ*, 370, 630
- Bliss, J., Arcones, A., Montes, F., & Pereira, J. 2020, *PhRvC*, 101, 055807
- Boggs, S. E., Harrison, F. A., Miyasaka, H., et al. 2015, *Sci*, 348, 670
- Buckby, M. A., & King, J. D. 1983, *JPhG*, 9, 85
- Cavanna, F., Depalo, R., Aliotta, M., et al. 2015, *PhRvL*, 115, 252501
- Chen, J., Singh, B., & Cameron, J. A. 2011, *NDS*, 112, 2357
- Cheng, C., & King, J. 1979, *JPhG*, 5, 1261
- Chieffi, A., & Limongi, M. 2013, *ApJ*, 764, 21
- Chieffi, A., & Limongi, M. 2017, *ApJ*, 836, 79
- Cybur, R. H., Amthor, A. M., Ferguson, R., et al. 2010, *ApJS*, 189, 240
- Cybur, R. H., Amthor, A. M., Heger, A., et al. 2016, *ApJ*, 830, 55
- deBoer, R. J., Görres, J., Wiescher, M., et al. 2017, *RvMP*, 89, 035007
- Diehl, R., & Timmes, F. X. 1998, *PASP*, 110, 637
- Eriksen, K. A., Arnett, D., McCarthy, D. W., & Young, P. 2009, *ApJ*, 697, 29
- Ertl, T., Janka, H. T., Woosley, S. E., Sukhbold, T., & Ugliano, M. 2016, *ApJ*, 818, 124
- Farmer, R., Fields, C. E., Petermann, I., et al. 2016, *ApJS*, 227, 22
- Fowler, W. A., & Hoyle, F. 1964, *ApJS*, 9, 201
- Fryer, C. L., Andrews, S., Even, W., Heger, A., & Safi-Harb, S. 2018, *ApJ*, 856, 63
- Fryer, C. L., Belczynski, K., Wiktorowicz, G., et al. 2012, *ApJ*, 749, 91
- Gibbons, J. H., & Macklin, R. L. 1959, *PhRv*, 114, 571
- Glebbeek, E., Gaburov, E., de Mink, S. E., Pols, O. R., & Portegies Zwart, S. F. 2009, *A&A*, 497, 255
- Goriely, S., Hilaire, S., & Koning, A. J. 2008, *PhRvC*, 78, 064307
- Grebenov, S. A., Lutovinov, A. A., Tsygankov, S. S., & Winkler, C. 2012, *Natur*, 490, 373
- Grefenstette, B. W., Harrison, F. A., Boggs, S. E., et al. 2014, *Natur*, 506, 339
- Harris, J. A., Hix, W. R., Chertkow, M. A., et al. 2017, *ApJ*, 843, 2
- Hix, W. R., & Thielemann, F.-K. 1999, *ApJ*, 511, 862
- Hoffman, R. D., Sheets, S. A., Burke, J. T., et al. 2010, *ApJ*, 715, 1383
- Hoffman, R. D., Woosley, S. E., Weaver, T. A., Rauscher, T., & Thielemann, F. K. 1999, *ApJ*, 521, 735
- Howard, A. J., Jensen, H. B., Rios, M., Fowler, W. A., & Zimmerman, B. A. 1974, *ApJ*, 188, 131
- Jerkstrand, A., Fransson, C., & Kozma, C. 2011, *A&A*, 530, A45
- Junde, H., Su, H., & Dong, Y. 2011, *NDS*, 112, 1513
- Kennett, S., Mitchell, L., Anderson, M., & Sargood, D. 1981, *NuPhA*, 363, 233
- Koo, B.-C., Kim, H.-J., Oh, H., et al. 2020, *NatAs*, 4, 584
- Limongi, M., & Chieffi, A. 2003, *ApJ*, 592, 404
- Longland, R., Dermigny, J., & Marshall, C. 2018, *PhRvC*, 98, 025802
- Lyons, S., Görres, J., deBoer, R. J., et al. 2018, *PhRvC*, 97, 065802
- Maeder, A., & Meynet, G. 2001, *A&A*, 373, 555
- Magkotsios, G., Timmes, F. X., Hungerford, A. L., et al. 2010, *ApJS*, 191, 66
- Magkotsios, G., Timmes, F. X., Wiescher, M., et al. 2008, in Proc. of the 10th Symp. on Nuclei in the Cosmos (NIC X), E112
- Meyer, B. S. 1994, *ARA&A*, 32, 153
- Mitchell, L., Kavanagh, R., Sevier, M., Tingwell, C., & Sargood, D. 1985, *NuPhA*, 443, 487
- Mohr, P. 2015, *EPJA*, 51, 56
- Müller, T., Prieto, J. L., Pejcha, O., & Clocchiatti, A. 2017, *ApJ*, 841, 127
- Newton, J. R., Iliadis, C., Champagne, A. E., et al. 2007, *PhRvC*, 75, 045801
- Nieuwenhuijzen, H., & de Jager, C. 1990, *A&A*, 231, 134
- Nomoto, K. 2014, in IAU Symp. 296, Supernova Environmental Impacts, ed. A. Ray & R. A. McCray (Cambridge: Cambridge Univ. Press), 27
- Nugis, T., & Lamers, H. J. G. L. M. 2000, *A&A*, 360, 227
- Ohio Supercomputer Center 1987, Ohio Supercomputer Center, <http://osc.edu/ark:/19495/f5s1ph73>
- Paxton, B., Bildsten, L., Dotter, A., et al. 2011, *ApJS*, 192, 3
- Paxton, B., Cantiello, M., Arras, P., et al. 2013, *ApJS*, 208, 4
- Paxton, B., Schwab, J., Bauer, E. B., et al. 2018, *ApJS*, 234, 34
- Paxton, B., Smolec, R., Schwab, J., et al. 2019, *ApJS*, 243, 10
- Paxton, B., Marchant, P., Schwab, J., et al. 2015, *ApJS*, 220, 15
- Pereira, J., & Montes, F. 2016, *PhRvC*, 93, 034611
- Pérez-Rendón, B., García-Segura, G., & Langer, N. 2002, *RMxAC*, 12, 94
- Plag, R., Reifarth, R., Heil, M., et al. 2012, *PhRvC*, 86, 015805
- Rauscher, T. 2010, *PhRvC*, 81, 045807
- Rauscher, T., Heger, A., Hoffman, R. D., & Woosley, S. E. 2002, *ApJ*, 576, 323
- Rauscher, T., Thielemann, F.-K., & Kratz, K.-L. 1997, *PhRvC*, 56, 1613
- Robertson, D., Görres, J., Collon, P., Wiescher, M., & Becker, H.-W. 2012, *PhRvC*, 85, 045810
- Rolf, C., Rodne, W., Shapiro, M., & Winkler, H. 1975, *NuPhA*, 241, 460
- Rolf, C. E., & Rodney, W. S. 1988, *Theoretical Astrophysics* (Chicago, IL: Univ. Chicago Press), 160
- Sawada, R., & Maeda, K. 2019, *ApJ*, 886, 47
- Scott, A., Morton, A., Tims, S., Hansper, V., & Sargood, D. 1993, *NuPhA*, 552, 363
- Seitenzahl, I. R., Timmes, F. X., & Magkotsios, G. 2014, *ApJ*, 792, 10
- Siebert, T., Diehl, R., Krause, M. G. H., & Greiner, J. 2015, *A&A*, 579, A124
- Sonzogni, A. A., Rehm, K. E., Ahmad, I., et al. 2000, *PhRvL*, 84, 1651
- The, L.-S., Clayton, D. D., Jin, L., & Meyer, B. S. 1998, *ApJ*, 504, 500
- Tims, S., Morton, A., Tingwell, C., et al. 1991, *NuPhA*, 524, 479
- Tur, C., Heger, A., & Austin, S. M. 2010, *ApJ*, 718, 357
- Vartanyan, D., Burrows, A., Radice, D., Skinner, M. A., & Dolence, J. 2019, *MNRAS*, 482, 351
- Vink, J. S., de Koter, A., & Lamers, H. J. G. L. M. 2001, *A&A*, 369, 574
- Vlieks, A., Cheng, C., & King, J. 1978, *NuPhA*, 309, 506
- Vlieks, A., Morgan, J., & Blatt, S. 1974, *NuPhA*, 224, 492
- Wagoner, R. V. 1969, *ApJS*, 18, 247
- Wang, T. R., Vogelaar, R. B., & Kavanagh, R. W. 1991, *PhRvC*, 43, 883
- Wang, W., & Li, Z. 2016, *ApJ*, 825, 102
- Wongwantharat, A., Janka, H., Müller, E., Pllumbi, E., & Wanajo, S. 2017, *ApJ*, 842, 13
- Woosley, S., & Janka, T. 2005, *NatPh*, 1, 147
- Woosley, S. E., Arnett, W. D., & Clayton, D. D. 1973, *ApJS*, 26, 231
- Wrean, P. R., Brune, C. R., & Kavanagh, R. W. 1994, *PhRvC*, 49, 1205
- Young, P. A., & Fryer, C. L. 2007, *ApJ*, 664, 1033
- Young, P. A., Fryer, C. L., Hungerford, A., et al. 2006, *ApJ*, 640, 891